

Article

The Relationship between Annealing Temperatures and Surface Roughness in Shaping the Physical Characteristics of $\text{Co}_{40}\text{Fe}_{40}\text{B}_{10}\text{Dy}_{10}$ Thin Films

Chi-Lon Fern¹, Wen-Jen Liu², Chia-Chin Chiang³ , Yung-Huang Chang⁴, Yuan-Tsung Chen^{5,*} , Yu-Zhi Wang⁵, Jia-Wei Liu⁵, Shih-Hung Lin⁶ , Ko-Wei Lin¹ and Sin-Liang Ou⁷

¹ Department of Materials Science and Engineering, National Chung Hsing University, Taichung 40227, Taiwan; fengcl@yuntech.edu.tw (C.-L.F.); kwlin@dragon.nchu.edu.tw (K.-W.L.)

² Department of Materials Science and Engineering, I-Shou University, Kaohsiung 84001, Taiwan; jurgen@isu.edu.tw

³ Department of Mechanical Engineering, National Kaohsiung University of Science and Technology, Kaohsiung 80778, Taiwan; ccchiang@nkust.edu.tw

⁴ Bachelor Program in Industrial Technology, National Yunlin University of Science and Technology, 123 University Road, Section 3, Douliou, Yunlin 64002, Taiwan; changyhu@yuntech.edu.tw

⁵ Graduate School of Materials Science, National Yunlin University of Science and Technology, 123 University Road, Section 3, Douliou, Yunlin 64002, Taiwan; u1042141@gmail.com (Y.-Z.W.); a0987116766@gmail.com (J.-W.L.)

⁶ Department of Electronic Engineering, National Yunlin University of Science and Technology, 123 University Road, Section 3, Douliou, Yunlin 64002, Taiwan; isshokenmei@yuntech.edu.tw

⁷ Bachelor Program for Design and Materials for Medical Equipment and Devices, Da-Yeh University, Changhua 51591, Taiwan; slo@mail.dyu.edu.tw

* Correspondence: ytchen@yuntech.edu.tw; Tel.: +886-5-534-2601



Citation: Fern, C.-L.; Liu, W.-J.; Chiang, C.-C.; Chang, Y.-H.; Chen, Y.-T.; Wang, Y.-Z.; Liu, J.-W.; Lin, S.-H.; Lin, K.-W.; Ou, S.-L. The Relationship between Annealing Temperatures and Surface Roughness in Shaping the Physical Characteristics of $\text{Co}_{40}\text{Fe}_{40}\text{B}_{10}\text{Dy}_{10}$ Thin Films. *Coatings* **2023**, *13*, 1895. <https://doi.org/10.3390/coatings13111895>

Academic Editor: Octavian Buiu

Received: 18 October 2023

Revised: 27 October 2023

Accepted: 3 November 2023

Published: 5 November 2023



Copyright: © 2023 by the authors. Licensee MDPI, Basel, Switzerland. This article is an open access article distributed under the terms and conditions of the Creative Commons Attribution (CC BY) license (<https://creativecommons.org/licenses/by/4.0/>).

Abstract: $\text{Co}_{40}\text{Fe}_{40}\text{B}_{10}\text{Dy}_{10}$ thin films, with thicknesses varying between 10 nm and 50 nm, were grown on a Si(100) substrate. Subsequently, they underwent a 1 h annealing process in an Ar atmosphere at temperatures of 100 °C, 200 °C, and 300 °C. The oxide characteristic peaks of Dy_2O_3 (440), Co_2O_3 (422), and Co_2O_3 (511) were revealed by X-ray diffraction (XRD). The low-frequency alternating current magnetic susceptibility (χ_{ac}) decreases with frequency. Due to thickness and the anisotropy of the magnetic crystal, the maximum χ_{ac} and saturation magnetization values rise with thicknesses and annealing temperatures. As the thickness and heat treatment temperature rise, the values for resistivity and sheet resistance tend to fall. The results of atomic force microscopy (AFM) and magnetic force microscopy (MFM) show that average roughness (R_a) lowers as the annealing temperature increases, and the distribution of strip-like magnetic domain becomes more visible. As thickness and annealing temperature increase, there is a corresponding rise in surface energy. Nano-indentation testing shows that hardness initially decreases from 10 nm to 40 nm, followed by an increase at 50 nm. Notably, annealing at 300 °C leads to a significant hardening effect, marking the highest level of hardness observed. Young's modulus increased as thicknesses and annealing temperatures increased. The magnetic, electric, and adhesive characteristics of CoFeBdy films are highly dependent on surface roughness at various annealing temperatures.

Keywords: $\text{Co}_{40}\text{Fe}_{40}\text{B}_{10}\text{Dy}_{10}$ thin films; annealing treatment; surface roughness; magnetic domain; low-frequency alternating current magnetic susceptibility (χ_{ac}); optimal resonance frequency (f_{res}); surface energy; adhesion; nano-indentation

1. Introduction

The development of magnetic recordings has long been the trend in information storage. The advancement of semiconductor technology has facilitated the development of numerous low-cost, high-performance information storage systems, such as magnetic

random access memory (MRAM), static random access memory (SRAM), and flash memory [1–3]. Spin-transfer moment magnetic random access memory (STT-MRAM) has recently been recognized as the next generation of reliable MRAM due to its excellent thermal stability, non-volatility, low write power, and low-frequency switching current [4]. The magnetic tunnel junction (MTJ) is the basic storage unit of MRAM. It comprises an insulating barrier layer situated between two ferromagnetic metal layers [5,6]. The tunneling magnetoresistance (TMR) ratio of MTJ, critical switching current density of magnetization, power consumption, and other features are all strongly related to the ferromagnetic layer type and structure, as well as the preparation procedure [7,8]. The best options for ferromagnetic layers are soft magnetic materials with high saturation magnetization (M_s) strength, high Curie temperature (T_c), low coercivity (H_c), high permeability (μ), and low magnetostriction (λ_s) in order to achieve magnetization reversal at a low energy cost. Particularly, it has been widely reported that MTJ performance can be enhanced by soft magnetic materials based on transition metals. Ellis and Elmen discovered the cobalt-iron (CoFe) alloy at an early stage [9]. Due to its favorable characteristics, such as high M_s , low H_c , and high μ , CoFe alloy has been studied by a large number of researchers [10]. However, when the annealing temperature reaches a critical level, the CoFe alloy experiences a loss of magnetic anisotropy, which prevents the magnetic component from functioning properly. As a result, boron (B) and dysprosium (Dy) are added to CoFe alloys as a third or fourth element. The mechanical properties and magnetic spin-exchanging coupling of B can be enhanced by grain refinement [11–13]. The magnetic thermal stability of a Dy doped alloy was enhanced [14,15]. The addition of an additional or third element can result in the formation of nanocomposite materials, which can improve specific features [16–22].

Over the past few decades, there has been a growing interest in the extraction and reclamation of rare earth elements (REs) due to their critical role in various industrial applications [23]. Currently, researchers are exploring the impact of incorporating RE ions, including Dy, gadolinium (Gd), ytterbium (Yb), lanthanum (La), and cerium (Ce), on the structural, magnetic, optical, and electrical properties of magnetic ferrite thin films [24–27]. As a result, introducing a third element to improve the distinct attributes can solve the problem of efficiency for diverse application contexts. According to literature studies, rare earth addition induces modifications in the microstructure, phase composition, and magnetic performance of the CoFe material [28,29]. Within MTJ configurations, CoFeB thin films are routinely incorporated, serving as either a free or pinned layer, and their contribution is vital for achieving a substantial TMR ratio [30,31]. The thickness selection is investigated in the range of 10–50 nm when the free layer or pinned layer thickness is typically quite thin [32]. Substituting a CoFeB seed or buffer layer with CoFeBDy films significantly enhances the thermal stability of these materials, making them a more viable choice for real-world MTJ applications. Additionally, annealing of magnetic components is typically carried out at temperatures near 350 °C, a critical factor in assessing their ability to withstand thermal stress [33]. In this study, it was chosen to investigate a temperature range from 100 °C to 300 °C, with 100 °C intervals, to evaluate the maintenance of magnetic properties. This approach aligns with our team's previous research conducted at the same annealing temperature. It is crucial to consider the nature of the material under examination when determining the suitable annealing temperature. For the aforementioned reasons, it is crucial to research the distinct properties and thermal stability of CoFeBDy films at annealed temperatures ranging from 100 °C to 300 °C. The primary approach in this study involved employing a uniform B/Dy ratio for the fabrication of CoFeBDy films, with the aim of improving magneto-thermal stability and several key physical attributes.

This study aims to assess the structural and magnetic properties of CoFeBDy thin films in relation to their thickness. Additionally, it explores the behavior of annealed CoFeBDy thin films at elevated temperatures. Given these considerations, investigating the incorporation of a third or fourth element, like Dy and B, into the CoFe alloy is a worthwhile avenue of exploration. It is profitable to invest in the unique qualities of CoFeBDy films by adding Dy and B into CoFe alloys. Surface roughness is a significant factor to take

into account when using the magnetic component at both room temperature (RT) and during annealing processes. It exerts a substantial impact on the physical properties of ultrathin films. Roughness has been studied in terms of magnetic, electrical, and optical qualities by researchers [34–37]. The novelty of this study lies in the introduction of Dy and B into CoFe alloy, forming quaternary alloys, and the exploration of surface roughness. This research aims to elucidate the relationship between surface energy and the magnetic properties of CoFeBDy thin films at varying thicknesses and under different annealing temperatures. $\text{Co}_{40}\text{Fe}_{40}\text{Dy}_{10}\text{B}_{10}$ was deposited onto a Si(100) substrate with a thickness of 10–50 nm and then annealed at 100, 200, and 300 °C in this work. Finally, following the established parameters, the study comprehensively investigated the film's structure, magnetic properties, surface energy, and nano-mechanical features post-annealing. Moreover, a significant endeavor has been made to explore the interplay between surface energy and magnetic properties at different thicknesses and during various annealing temperatures of CoFeDyB thin films.

2. Materials and Methods

Sputtering and annealing conditions: CoFeBDy thin films, with thicknesses ranging from 10 to 50 nm, were fabricated on a Si(100) substrate using direct current (DC) magnetron sputtering. The Si(100) substrate is square-shaped, with dimensions of 1 cm on each side and a thickness of 1 mm. The films were fabricated under four distinct conditions: room temperature (RT), subsequent annealing at 100 °C for 1 h, subsequent annealing at 200 °C for 1 h, and subsequent annealing at 300 °C for 1 h. It featured a 1.65 W/cm^2 power density and a 50 W sputtering power. The chamber base pressure was 3.54×10^{-7} Torr, while the working pressure for the Ar gas was 3.09×10^{-3} Torr. The loader rotated at 20 rpm and the flow rate of the Ar gas was 20 sccm. Following deposition, the samples were subjected to controlled annealing for 1 h, with temperatures ranging from 100 °C to 300 °C and controlled heating rates of 30 °C/min, accompanied by cooling rates of 0.5 °C/min. Throughout the annealing process, the vacuum chamber pressure was consistently held at 2.5×10^{-3} Torr.

Compositions: A new chemical element CoFeBDy alloy has appeared, consisting of 40% Co, 40% Fe, 10% B, and 10% Dy. The CoFeBDy target is a commercially manufactured alloy sourced from pure metals supplied by Gredmann Taiwan Ltd. The target is positioned 30 cm away from the substrate and has dimensions of 2 mm in thickness and 3 inches in diameter. To create the desired composition, a powder mixture consisting of 99.9% pure elements Co, Fe, B, and Dy was prepared. The target's composition ratio has been validated through original factory certification for composition testing. Any disparity between the target's composition and the actual composition arises due to Ar ion bombardment and sputter deposition ion angles [38].

Techniques and characterizations: The structure of the CoFeBDy thin films was analyzed using Grazing Incidence X-ray Diffractometer (GIXRD) patterns obtained from $\text{CuK}\alpha_1$ (Panalyticalx'pertPROMRD, Philips, Amsterdam, The Netherlands) and low-angle diffraction incidence, approximately 2°. Energy dispersive X-ray spectroscopy (EDS, Zeiss, UltraPlus, Oberkochen, Baden-Württemberg, Germany) was employed for elemental composition analysis of the thin films. The structure of the CoFeBDy thin films was examined through Grazing Incidence X-ray Diffractometer (GIXRD) patterns acquired using $\text{CuK}\alpha_1$ (Panalyticalx'pertPROMRD) and low-angle diffraction at around 2°. Elemental composition analysis of the thin films was conducted using energy dispersive X-ray Spectroscopy (EDS, Zeiss, UltraPlus) system. Using a low-frequency alternate-current magnetic susceptibility (χ_{ac}) analyzer (MagQu, acQuan II, New Taipei City, Taiwan), the χ_{ac} of $\text{Co}_{40}\text{Fe}_{40}\text{B}_{10}\text{Dy}_{10}$ thin films was examined. Measurement of the external magnetic field 50 mG, χ_{ac} was used to calibrate standard sample. Testing of the samples was performed using a χ_{ac} analyzer, with a frequency range spanning from 10 Hz to 25,000 Hz, and χ_{ac} was determined based on the magnetization strength. To prevent demagnetization, all samples are the exact same size $0.5 \text{ cm} \times 0.5 \text{ cm}$ and square form. Since the exchange results are comparisons to the

samples that serve as the reference standard, the χ_{ac} values are expressed in arbitrary units (a.u.). The frequency of the highest χ_{ac} is found by the χ_{ac} analyzer by finding the best resonance frequency (f_{res}). The hysteresis loop of the CoFeBDy films was assessed using a vibrating sample magnetometer (VSM, NanoMagnetics, Banbury, UK). Atomic force microscopy (AFM, NanoMagnetics Instruments, ezAFM, Banbury, UK) was employed to evaluate the surface morphology of the films, and magnetic force microscopy (MFM) was used to characterize the magnetic domains of the films. AFM is assessed in non-contact mode with average area evaluation using three scanning repeats at RT. It is used Ra to measure roughness. Ra is a shortened term representing the arithmetic mean deviation, which was employed to evaluate the surface area. $20 \mu\text{m} \times 20 \mu\text{m}$ is the size of the scanning. The precise thickness was additionally calibrated using AFM and the height difference approach. Through the use of a Four Point Probe Tester (Sadhudesign, Hsinchu City, Taiwan), the correlation between electrical resistance and film thickness was found. Deionized (DI) water and glycerin were used to measure the contact angle. Every contact angle measurement was conducted three times to ensure precision, and the resulting average contact angles were then calculated. A contact angle measuring device (CAM-110) from Creating Nano Technologies in Tainan City, Taiwan, was utilized to gauge the contact angle, facilitating the calculation of surface energy [39–41]. The hardness (H) and Young's modulus (E) of $\text{Co}_{40}\text{Fe}_{40}\text{B}_{10}\text{Dy}_{10}$ films were measured using an MTS (Mechanical Testing & Simulation) Nano Indenter XP (MTS, Minneapolis, MN, USA) with a Berkovich tip and the continuous stiffness measurement (CSM) technique. After the load has been decreased to 10% of its maximum value, withdrawing the indentation from the surface at the same rate followed. Each sample was subjected to ten repetitions of measurements using the probe. The indentation load was incrementally increased over 40 stages, and the indentation depth was recorded at each increment. Six indentations from each sample were analyzed, and the averaged standard deviations were used to enhance the accuracy of the statistical data. The mechanical characteristics were computed using Oliver and Pharr's method.

3. Results

3.1. XRD Structure Property, Full Width of Half Maximum, and Composition Analysis

Figure 1a–d show the X-ray diffraction (XRD) results for the analysis of the as-deposited and annealed $\text{Co}_{40}\text{Fe}_{40}\text{B}_{10}\text{Dy}_{10}$ films. From the literature, it was determined that the crystalline phases of $\text{Co}_{40}\text{Fe}_{40}\text{B}_{10}\text{Dy}_{10}$ were represented by three metal oxide signature peaks, which may be Dy_2O_3 (440), Co_2O_3 (422), and Co_2O_3 (511), respectively, at $2\theta = 47.8^\circ$, 54.65° , and 56.45° [42,43]. Even after reaching a vacuum level as low as 10^{-7} Torr, it is possible for residual oxygen to remain within the sputtering chamber. The emergence of oxidation peaks is ascribed to a combination of naturally occurring oxides present on the Si(100) substrate and oxygen contamination on the sputtering target [44]. The presence of oxides can be inferred from the affinities and negativities between each element and oxygen [45]. According to Figure 1a–d, the total oxide peak intensities exhibited a distinct decrease with increasing CoFeBDy thickness and annealing temperature. Conversely, a decrease in film thickness led to an increase in the amount of oxides, as the oxidation degree remained fairly uniform across various film thicknesses. Consequently, with the increase in thickness and annealing temperature, the intensity of the oxide peaks exhibited a continuous decline. As a result, the interference from the oxide peak is reduced, and the film's electrical and magnetic properties are enhanced.

Figure 2a,b illustrate the FWHM and intensity of diffracted peaks from the overall oxides, underscoring the pronounced influence of lower annealing temperatures on oxidation compared to higher annealing temperatures. The points in Figure 2 represent the FWHM and XRD diffraction intensity of all oxides and thicknesses under various annealing conditions. It is evident that lower annealing temperatures result in narrower FWHM values and higher XRD intensities, highlighting the substantial impact of oxidation in these specific conditions.

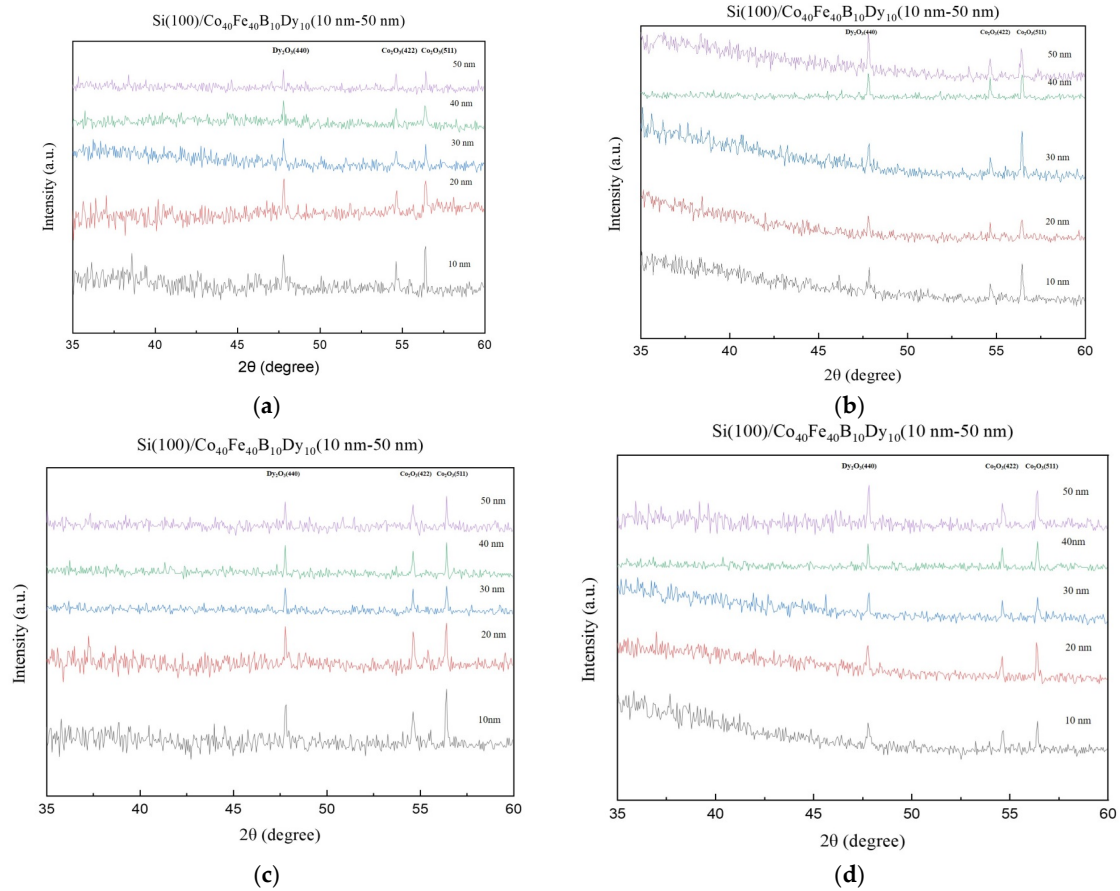


Figure 1. The XRD patterns for $\text{Co}_{40}\text{Fe}_{40}\text{B}_{10}\text{Dy}_{10}$ films were recorded under various conditions: (a) at RT, (b) post-annealing at $100\text{ }^{\circ}\text{C}$, (c) following annealing at $200\text{ }^{\circ}\text{C}$, and (d) after annealing at $300\text{ }^{\circ}\text{C}$.

The composition of the CoFeBDy alloy films was assessed at a thickness of 50 nm. Figure 3 presents both the composition data and the corresponding EDS pattern generated by an EDS spectrometer for the CoFeBDy films. Nonetheless, the EDS analysis could not ascertain the B content due to the lightweight nature of boron atoms. The dispersion of sputtered atoms in multiple directions and angles leads to compositional non-uniformity [46]. The loss of atom content during film growth is caused by the bombardment of argon ions during sputtering deposition, and the actual elemental composition of the samples differs significantly from nominal $\text{Co}_{40}\text{Fe}_{40}\text{Dy}_{10}\text{B}_{10}$ in this way [47]. The target and obtained compositions are also significantly different from one another, which results in a greater contribution of Co atoms. According to XRD result, the Co is produced to Co_2O_3 oxide and decreased the magnetic property.

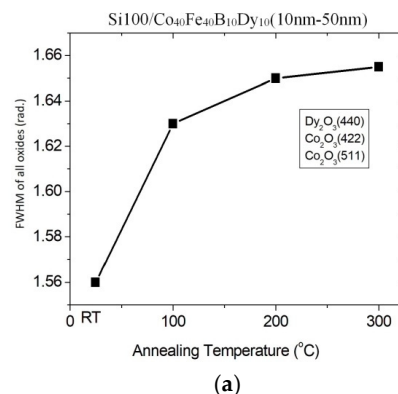


Figure 2. Cont.

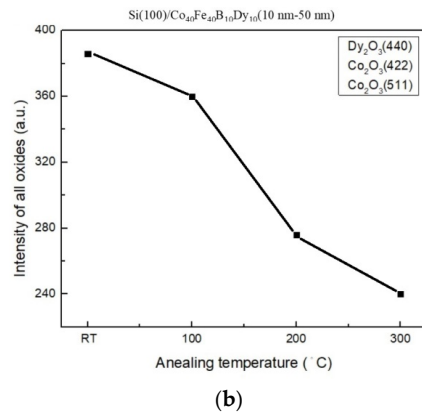


Figure 2. XRD analysis of total oxide peaks in $\text{Co}_{40}\text{Fe}_{40}\text{B}_{10}\text{Dy}_{10}$ films under different conditions. (a) FWHM and (b) XRD diffracted peak intensity.

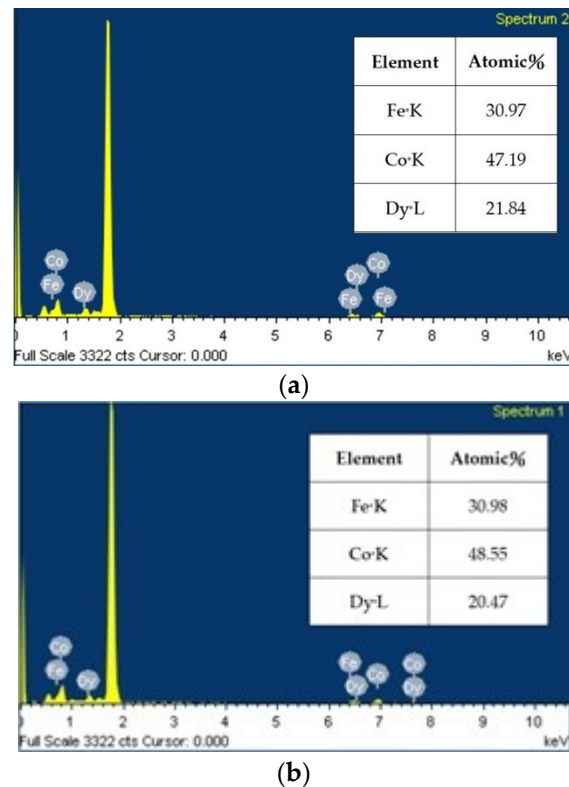
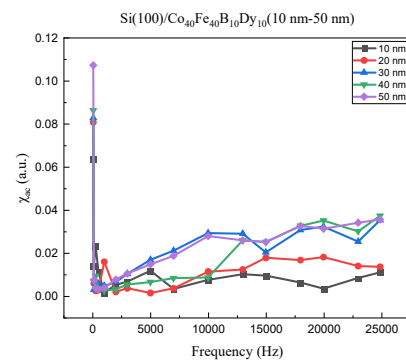


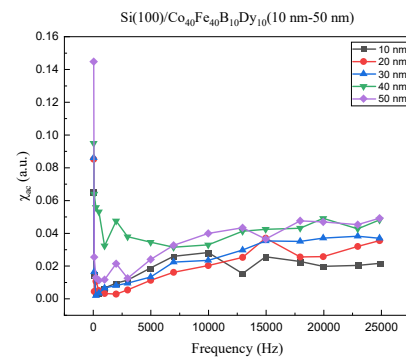
Figure 3. EDS patterns of $\text{Co}_{40}\text{Fe}_{40}\text{B}_{10}\text{Dy}_{10}$ thin films. (a) RT and (b) annealing 300 °C.

3.2. Magnetic Properties

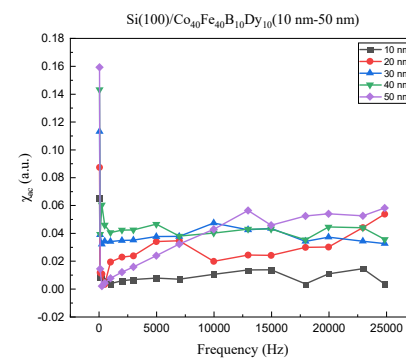
Figure 4a–d display the low-frequency alternating-current magnetic susceptibility (χ_{ac}) values of the films at RT and after annealing at 100 °C, 200 °C, and 300 °C. The graphs show that χ_{ac} values of the $\text{Co}_{40}\text{Fe}_{40}\text{B}_{10}\text{Dy}_{10}$ films, with or without heat treatment, exhibit an upward tendency. The susceptibility peaks provide insights into the occurrence of magnetic exchange coupling and spin sensitivity, particularly pronounced at low frequencies. This holds profound physical significance. In the low-frequency realm, the alternating-current (AC) magnetic dipole moment primarily arises from the oscillation of the volume magnetic dipole moment within each domain. An applied AC magnetic field generates a driving force, reigniting magnetic interactions between domains. This results in a resonant frequency within the system, and this resonant frequency correlates with the oscillation of the magnetic dipole moment within domains, intimately connected to the frequency of the low-frequency magnetic susceptibility peak. Hence, the χ_{ac} peak signifies the presence of spin exchange-coupling interactions and the dipole moment of the frequency domain [48].



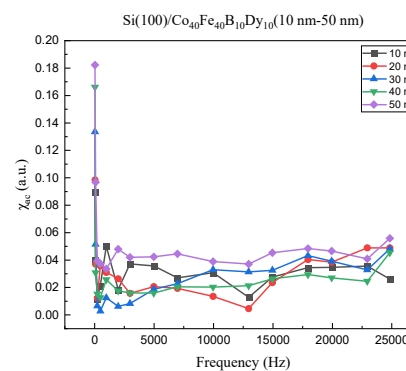
(a)



(b)



(c)



(d)

Figure 4. χ_{ac} at low frequencies was measured for $\text{Co}_{40}\text{Fe}_{40}\text{B}_{10}\text{Dy}_{10}$ films under the following conditions: (a) at RT, (b) after annealing at 100 °C, (c) following annealing at 200 °C, and (d) subsequent to annealing at 300 °C.

Figure 5 illustrates that by increasing the thickness of the film deposition, the maximum χ_{ac} value can be attained, and, following heat treatment, the χ_{ac} value shows a noticeable increase. At an annealing temperature of 300 °C, a maximum χ_{ac} value of 0.18 is achieved for a 50 nm thickness. Comparatively, at RT, the χ_{ac} value is 0.10 for 50 nm, 0.14 for 50 nm at 100 °C, and 0.15 for 50 nm at 200 °C. This increase in the maximum χ_{ac} value is attributed to both thickness and the magneto-crystalline anisotropy effect [49–51]. The graph illustrates that the Si(100) substrate exhibits its peak χ_{ac} value at the resonance frequency of 50 Hz. However, with an increase in measurement frequency, there is a discernible decline in χ_{ac} values, likely stemming from the anisotropy inherent in the magnetic crystals [52].

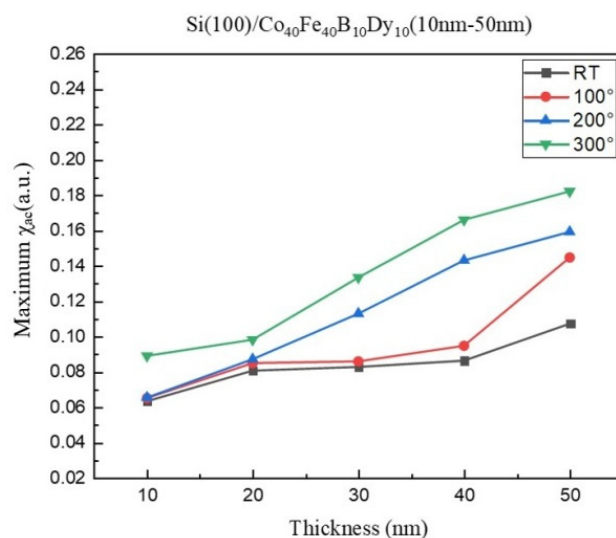


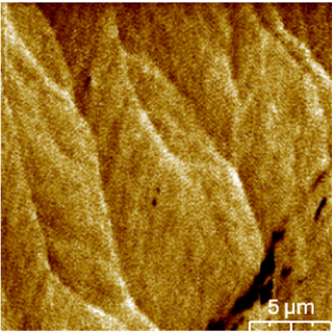
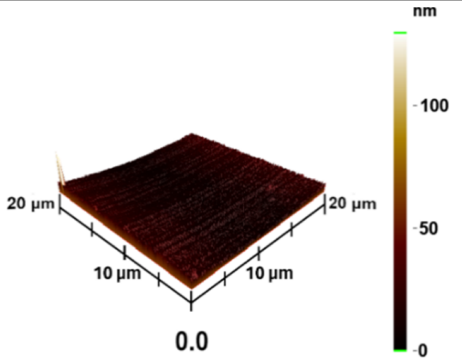
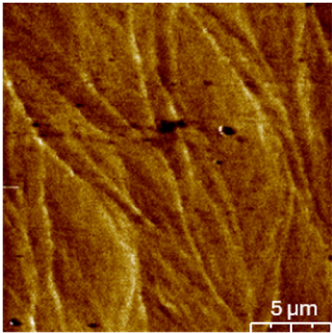
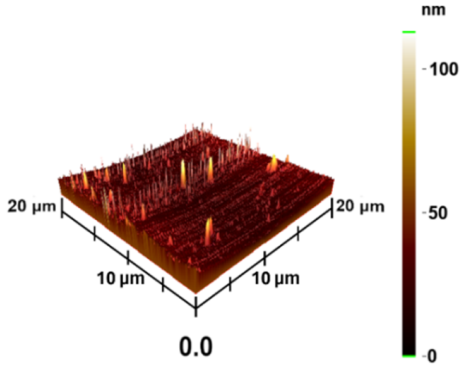
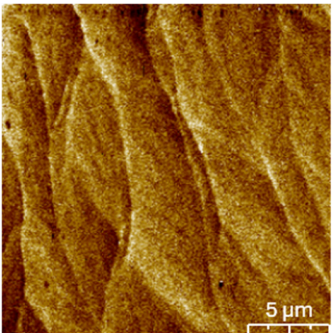
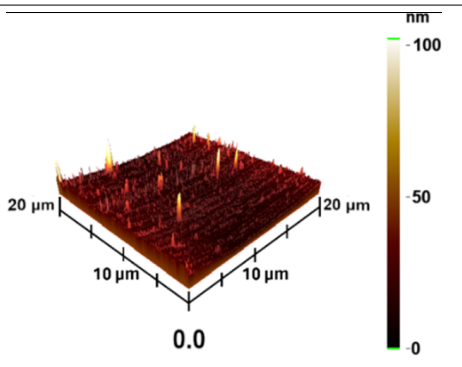
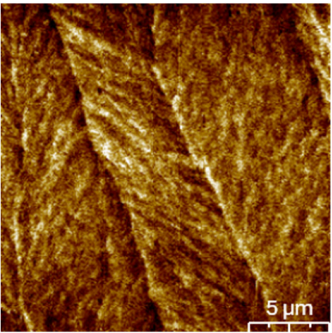
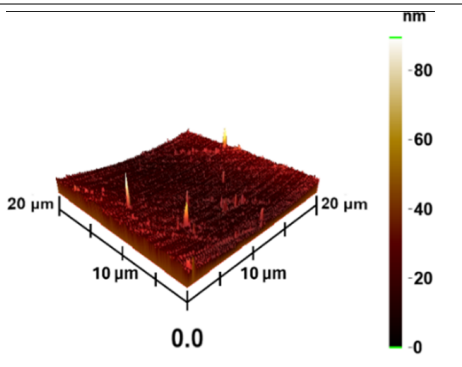
Figure 5. Maximum χ_{ac} at different temperatures.

VSM carried out the in-plane hysteresis loop for 50 nm $\text{Co}_{40}\text{Fe}_{40}\text{B}_{10}\text{Dy}_{10}$ films. In-plane hysteresis loops for 50 nm $\text{Co}_{40}\text{Fe}_{40}\text{B}_{10}\text{Dy}_{10}$ films are shown in Figure 6a, and the plot of coercivity and saturation magnetization at different annealing temperatures is shown in Figure 6b. Based on the results, the interplay of thickness and magnetic crystal anisotropy led to an increase in the H_c and M_s values, transitioning from 6 Oe to 16 Oe and 603 emu/cm^3 to 810 emu/cm^3 as the annealing temperatures escalated from RT to 300 °C [49–52]. Additionally, the H_c displays a lower value and suggests that $\text{Co}_{40}\text{Fe}_{40}\text{B}_{10}\text{Dy}_{10}$ films have a soft magnetic. The $\text{Co}_{40}\text{Fe}_{40}\text{B}_{10}\text{Dy}_{10}$ films with a thickness of 50 nm that were annealed at 300 °C had low H_c and relatively high M_s , which led to enhanced soft magnetic characteristics. These films are ideal for spintronics, microactuators, magnetic memory, and storage devices.

Figure 7a,b present the findings for resistivity and sheet resistance across various conditions. The results reveal that as thickness and annealing temperatures decrease, there is a substantial increase in resistivity and sheet resistance, primarily due to the oxidation effect associated with thinner thickness. Typically, finer grain distribution and increased grain boundaries are characteristics of thinner films [53,54]. Because thinner films and lower annealing temperatures have a higher proportion of oxides and grain boundaries, which impair current carrier transport and raise resistivity and sheet resistance, they also have thinner films and lower annealing temperatures [55,56]. The findings show that the resistivity varied between 0.124 and $0.001 \Omega \text{ cm}$ while the sheet resistance varied between 12.36×10^4 and $0.014 \times 10^4 \Omega/\text{sq}$. In addition, it is known from the AFM experiments in Table 1 that the roughness decreases as the annealing temperature rises, the size of the internal grains increases, and there are fewer grain boundaries after the annealing, all of which will allow for easier current passage through the film and a consequent decrease in the value of the value measured [57,58]. Higher annealing temperatures result in reduced scattering of electrical carriers. Elevated annealing temperatures typically reduce the negative impact of defects on electrical properties. Moreover, one can reasonably infer that

when the mean free path of electrons approaches the film thickness, it becomes another potential contributor to heightened resistivity in extremely thin film [59].

Table 1. $\text{Co}_{40}\text{Fe}_{40}\text{B}_{10}\text{Dy}_{10}$ 50 nm films at different heat treatment temperatures with magnetic domain and surface roughness.

Temperature (°C)	Magnetic Domain	Surface Roughness (nm)	Average Roughness, Ra (nm)
RT			2.73 nm
100			2.49 nm
200			2.45 nm
300			1.84 nm

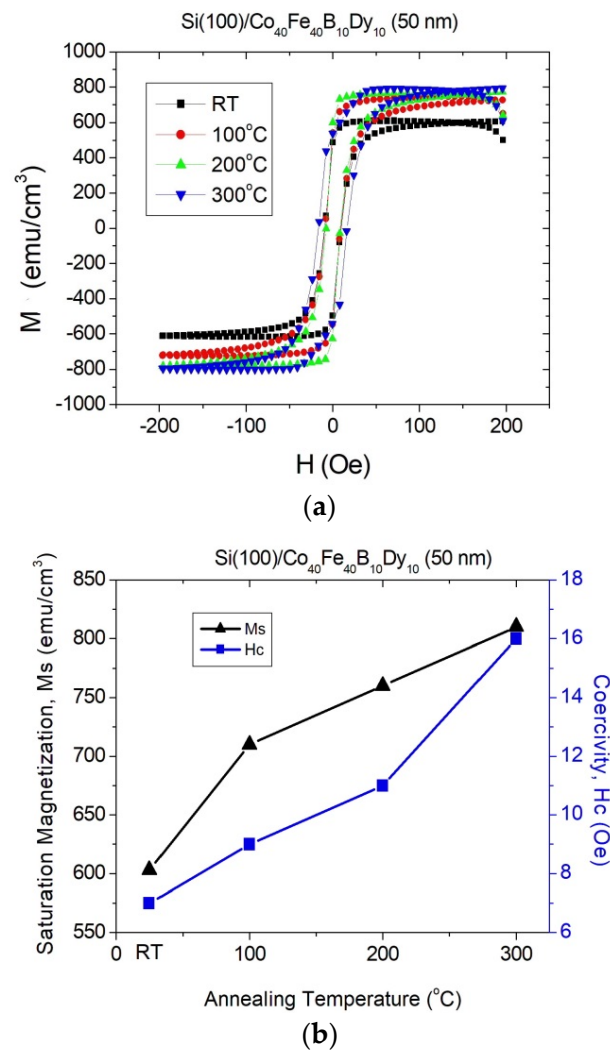


Figure 6. The in-plane magnetization of deposited and annealed $\text{Co}_{40}\text{Fe}_{40}\text{B}_{10}\text{Dy}_{10}$ 50 nm films. (a) In-plane hysteresis loop and (b) variations of H_c and M_s .

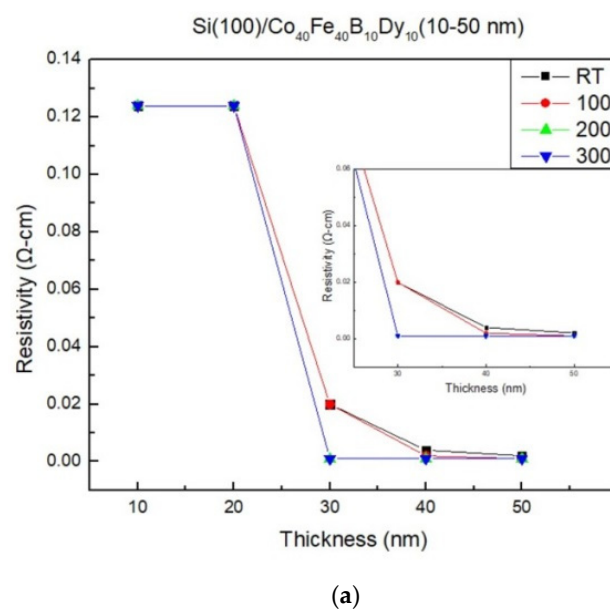
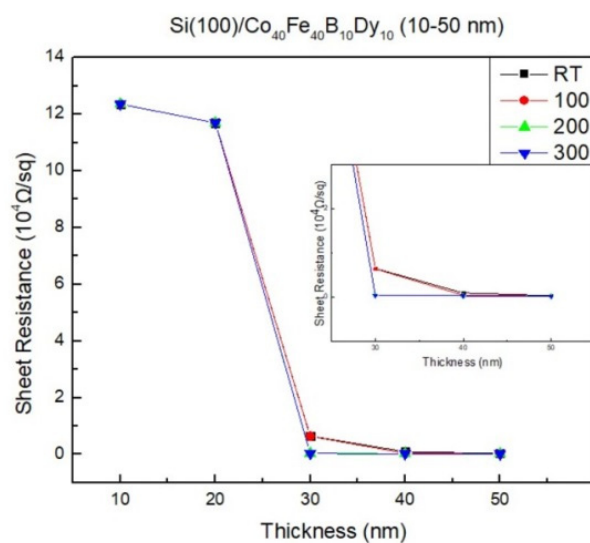


Figure 7. Cont.



(b)

Figure 7. The electrical properties of $\text{Co}_{40}\text{Fe}_{40}\text{B}_{10}\text{Dy}_{10}$ films. (a) Resistivity and (b) sheet resistance at RT, annealing 100 °C, 200 °C, and 300 °C.

3.3. Surface Roughness and Magnetic Domains

Table 1 depicts the magnetic domain and surface morphology at 50 nm for various circumstances. This measurement is based on the 50 nm, primarily because it aligns with the condition that yields the highest χ_{ac} value. This correlation implies that the distribution of magnetic domains is the most prominent feature in the image. The scanning range of the samples is $20 \mu\text{m} \times 20 \mu\text{m}$. The magnetic domain form of $\text{Co}_{40}\text{Fe}_{40}\text{B}_{10}\text{Dy}_{10}$ films exhibits a fine stripe feature. The average stripe magnetic domain increases about from 2 μm to 5 μm in width size when the annealing temperature is elevated to 300 °C. The features of domain structures are thought to have a substantial impact on magnetic behavior. The continuity and contrast of magnetic domains experience enhancements following the annealing of the film, primarily due to a slight improvement in exchange coupling [60,61]. The larger area of the magnetic domain produces stronger magnetization, which is consistent with the χ_{ac} result. The surface roughness is observed using 3D graphs, and it is observed that the surface roughness exhibits a slight improvement in smoothness. The average roughness (Ra) was measured in a flat region. The Ra value was 2.73 nm at room temperature and then reduced to 1.84 nm when the annealing temperature climbed to 300 °C. The contrast between the color depth and the area shown in the image determines the magnetic area pattern of the material. Maximum χ_{ac} and surface roughness have a link in the results of Figure 4 and Table 1, pointing towards the notion that increased surface roughness has the potential to induce the pinning of domain walls, thus impeding their movement and leading to a decrease in the χ_{ac} value [62,63]. Furthermore, an increase in annealing temperature results in diminished electric carrier scattering and mitigates the detrimental impact of defects on electrical properties. As a consequence, this leads to a reduction in both resistivity and sheet resistance.

3.4. Angle of Contact and Surface Energy

The contact angle measurements on a Si(100) substrate in both DI water and glycerol are showcased in Figure 8a–d. It is clear that as the thickness increases at the same annealing temperature, the contact angle consistently decreases. The contact angle likewise tends to decrease with increasing annealing temperature for the same thickness. The contact angles measured for the $\text{Co}_{40}\text{Fe}_{40}\text{B}_{10}\text{Dy}_{10}$ film in various solutions consistently register below 90°, confirming its hydrophilic characteristics. Surface roughness and grain size are identified as two key factors influencing these contact angles. This study demonstrates

that elevating the annealing temperature results in a decrease in surface roughness and a corresponding reduction in the contact angle during AFM measurements conducted at the same film thickness [64–66].

Figure 9 provides a visual representation of the variation in surface energy as the annealing temperature increases from RT to 300 °C. Notably, as both thickness and annealing temperature are heightened, the surface energy experiences an increase, attaining a higher level. The surface energy values range from 25.31 mJ/mm² to 32.38 mJ/mm². At 300 °C, 32.38 mJ/mm² was the surface energy with the greatest 50 nm. Stronger adhesion is observed when the films possess higher surface energy. Furthermore, it is essential to take into account both surface energy and adhesion, as the Co₄₀Fe₄₀B₁₀Dy₁₀ film can serve various roles, such as a seed or buffer layer, ensuring compatibility with other layer in double-layer and multi-layer systems. It can also function as a free or pinned layer, facilitating diverse magnetic processes. Increased surface energy enhances liquid absorption and reduces the contact angle. This effect arises from the stronger attraction between liquid molecules and solid atoms, surpassing the intermolecular forces within the liquid. Additionally, higher surface energy corresponds to lower surface tension in the liquid. Therefore, higher surface energy leads to easier wetting and better adhesion [67]. Because of this, the 50 nm Co₄₀Fe₄₀B₁₀Dy₁₀ film displayed better adhesive characteristics than the others after being annealed at 300 °C, which may theoretically be attributed to its less rough surface [68]. Overall, the surface roughness of CoFeBDy films at various annealing temperatures has a considerable impact on their magnetic, electric, and adhesive properties. It is simpler to shift and increase χ_{ac} value due to the less pinning impact of smoother roughness on domain walls. As a result of the diminished surface roughness, the contact angle decreases, and surface energy increases. Furthermore, rougher surfaces have a higher carrier conductivity, which reduced electrical resistance.

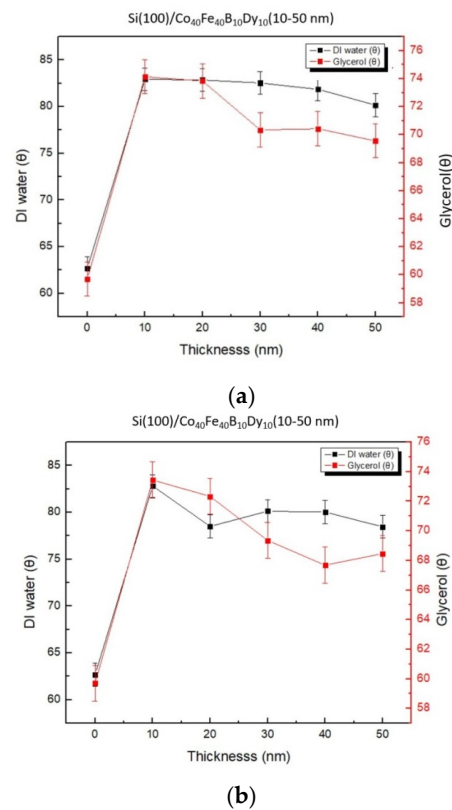


Figure 8. Cont.

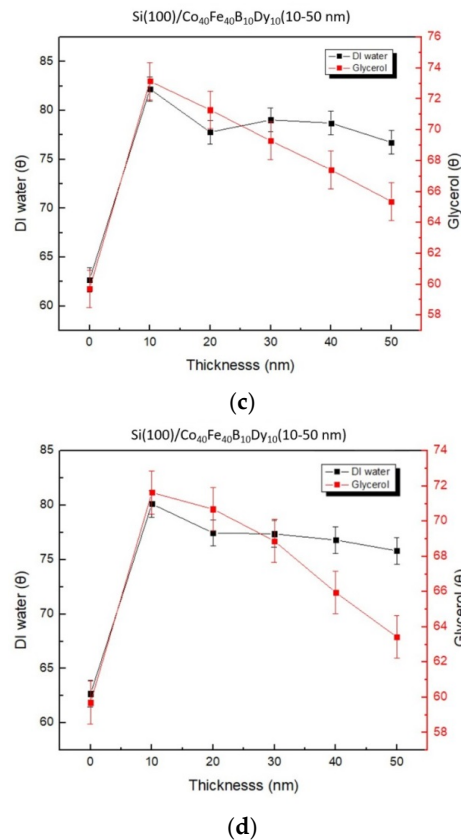


Figure 8. Contact angles for $\text{Co}_{40}\text{Fe}_{40}\text{B}_{10}\text{Dy}_{10}$ films were determined at various stages: (a) RT, (b) after annealing at 100 °C, (c) following annealing at 200 °C, (d) post-annealing at 300 °C.

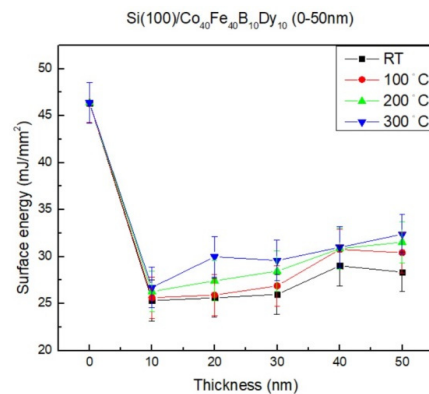


Figure 9. Surface energy of $\text{Co}_{40}\text{Fe}_{40}\text{B}_{10}\text{Dy}_{10}$ thin films.

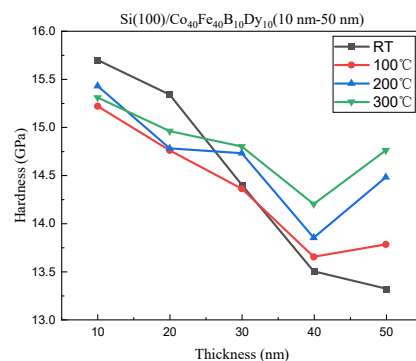
3.5. Hardness and Young’s Modulus

The hardness (H) and Young’s modulus (E) of $\text{Co}_{40}\text{Fe}_{40}\text{B}_{10}\text{Dy}_{10}$ films under various circumstances are shown in Figure 10a,b. The maximum hardness is 15.7 GPa at 10 nm at RT, while the minimum hardness is 13.32 GPa at 50 nm at RT. While the thickness of deposition increases from 10 nm to 40 nm, the hardness tends to decrease, but it experiences a subsequent hardening when the thickness reaches 50 nm. Due to the presence of Dy, Young’s modulus tends to increase with thickness and annealing temperature. Furthermore, as an XRD result, Dy is generated as Dy_2O_3 oxide. The amount of Dy_2O_3 could refine the grains and contribute to hardness and Young’s modulus [69]. At 50 nm and 300 °C annealing, the maximal Young’s modulus is 200.1 GPa. At critical thickness of 40 nm, the hardness softens first before becoming harder. Reasonably speaking, it can be deduced that the film preserves its hardness at a particular annealing temperature and that the hardness hardens as a result of the recovery of defects during the heat treatment [70]. The

phenomenon of enhanced strength at elevated firing temperatures, particularly when the film measures 50 nm in thickness, finds its explanation in the realms of materials science and thin-film physics. This effect is primarily a consequence of the synergy between grain growth and defect annealing. A pivotal factor at play centers around the response of grains and defects within thin films to the application of elevated temperatures. As the film is subjected to higher temperatures, atoms gain greater mobility, facilitating the repair of defects. This annealing process serves to eradicate structural flaws, thereby bolstering the material’s strength [71]. The thickness of the film assumes a pivotal role in this process. Thicker films, particularly those exceeding 50 nm, possess a more substantial volume relative to their surface area. This increased volume provides a greater expanse for defects to diffuse and undergo annealing. Consequently, the material can recuperate from defects more effectively in thicker films, resulting in a notable increase in strength [72]. The magnetic and crystalline properties of Si(100)/Co₄₀Fe₄₀B₁₀Dy₁₀ films in both as-deposited and post-annealing states were compared with those of Glass/Co₄₀Fe₄₀B₁₀Dy₁₀, as detailed in Table 2 [73]. The results from Table 2 reveal a clear distinction. Glass/Co₄₀Fe₄₀B₁₀Dy₁₀ exhibits an amorphous structure, while Si(100)/Co₄₀Fe₄₀B₁₀Dy₁₀ displays a crystalline structure due to substrate effects [74]. Additionally, the maximum χ_{ac} similarity increases with thickness and annealing temperature, attributed to thickness effects and magneto-crystalline anisotropy. However, Si(100)/Co₄₀Fe₄₀B₁₀Dy₁₀ has a smaller maximum χ_{ac} compared to Glass/Co₄₀Fe₄₀B₁₀Dy₁₀ due to the presence of oxide peaks. Furthermore, an increase in surface energy and a reduction in surface roughness to 50 nm were noted with higher thickness and annealing temperature. In the context of applying our research to practical uses, this study has investigated how surface roughness and annealing temperature influence a promising magnetic material—namely, the Co₄₀Fe₄₀B₁₀Dy₁₀ thin film. An essential future consideration is its suitability as either the free or pinned layer in an MTJ structure. This research provides valuable reference data for the broader field of magnetism.

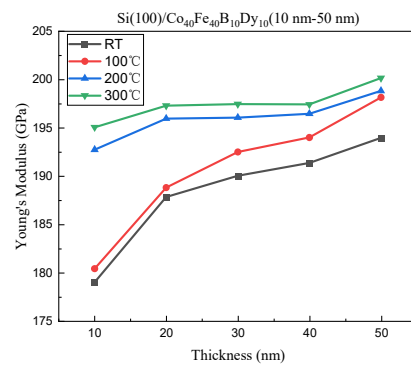
Table 2. Significant properties for Glass/Co₄₀Fe₄₀B₁₀Dy₁₀ and Si(100)/Co₄₀Fe₄₀B₁₀Dy₁₀ materials.

Material	Crystallinity	Maximum χ_{ac} (a.u.)	Resistivity (Ω -cm) and Sheet Resistance (Ω /sq)	Surface Energy (mJ/mm ²)	Surface Roughness, Ra (nm) at 50 nm with Various Conditions
Glass/Co ₄₀ Fe ₄₀ B ₁₀ Dy ₁₀ [73] 10–50 nm at RT and annealed conditions	Amorphous	0.14–0.18 at 50 nm	0.001–0.275 0.029×10^4 – 12.36×10^4	26.39–34.71	1.93–1.19
Si(100)/Co ₄₀ Fe ₄₀ B ₁₀ Dy ₁₀ 10–50 nm at RT and annealed conditions (current research)	Metal oxide signature peaks, Dy ₂ O ₃ (440), Co ₂ O ₃ (422), and Co ₂ O ₃ (511)	0.10–0.18 at 50 nm	0.001–0.124 0.014×10^4 – 12.36×10^4	25.31–32.38	2.73–1.84



(a)

Figure 10. Cont.



(b)

Figure 10. The nanomechanical properties of $\text{Co}_{40}\text{Fe}_{40}\text{B}_{10}\text{Dy}_{10}$ films. (a) Hardness and (b) Young's modulus of thin films at RT, annealing 100 °C, 200 °C, and 300 °C.

4. Conclusions

XRD presents that the oxide characteristic peaks of Dy_2O_3 (440), Co_2O_3 (422) and Co_2O_3 (511) with $2\theta = 47.8^\circ$, 54.65° , and 56.45° were generated in $\text{Co}_{40}\text{Fe}_{40}\text{B}_{10}\text{Dy}_{10}$ thin films at various annealing temperatures. Regardless of the heat treatment temperature, the film consistently exhibits its optimal resonance frequency at 50 Hz. However, as the measured frequency increases, there is a tendency for the χ_{ac} value to decline. The maximum χ_{ac} and M_s values exhibit an upward trend with increasing thickness and annealing temperature, primarily influenced by variations in thickness and magnetic crystal anisotropy. The magnetic domain of 50 nm grows larger with increasing annealing temperature, whereas the surface roughness of 50 nm grows smoother with increasing annealing temperature. To summarize, the magnetic, electrical, and adhesive properties of CoFeBDy films are significantly influenced by surface roughness at different annealing temperatures. A smoother surface with reduced roughness has a lesser impact on domain wall pinning, leading to enhanced mobility and, consequently, higher χ_{ac} values. Moreover, surface roughness correlates with a lower contact angle and increased surface energy. According to the study, the optimal condition is annealing at 300 °C with a film thickness of 50 nm.

Author Contributions: Conceptualization, C.-L.F., W.-J.L., Y.-H.C., Y.-T.C., S.-H.L. and S.-L.O.; Methodology, C.-L.F., Y.-T.C., Y.-H.C., Y.-Z.W., J.-W.L. and K.-W.L.; validation, formal analysis, Y.-Z.W., Y.-T.C., J.-W.L. and S.-L.O.; investigation, C.-L.F., Y.-T.C. and W.-J.L.; resources, C.-C.C. and K.-W.L.; writing—original draft preparation, Y.-T.C.; writing—review and editing, C.-L.F., Y.-T.C. and W.-J.L.; supervision, Y.-T.C. and Y.-H.C.; project administration, Y.-T.C. and S.-H.L.; funding acquisition, C.-L.F., C.-C.C. and Y.-H.C. All authors have read and agreed to the published version of the manuscript.

Funding: This work was supported by the National Science Council, under Grant No. MOST 110-2221-E-992-054 -MY3, MOST108-2221-E-224-015-MY3, MOST105-2112-M-224-001, and National Yunlin University of Science and Technology, under Grant No. 111T01 and 113T01.

Institutional Review Board Statement: Not applicable.

Informed Consent Statement: Not applicable.

Data Availability Statement: Not applicable.

Conflicts of Interest: The authors declare that there are no conflict of interests regarding the publication of this paper. The funders had no role in the design of the study; in the collection, analyses, or interpretation of data; in the writing of the manuscript, or in the decision to publish the results.

References

1. Selberherr, S.; Sverdlov, V. About electron transport and spin control in semiconductor devices. *Solid State Electron. Lett.* **2022**, *197*, 108443. [\[CrossRef\]](#)
2. Grezes, C.; Li, X.; Wong, K.L.; Ebrhami, F.; Amiri, P.K.; Wang, K.L. Voltage-controlled magnetic tunnel junctions with synthetic ferromagnet free layer sandwiched by asymmetric double MgO barriers. *J. Phys. D* **2019**, *53*, 014006. [\[CrossRef\]](#)
3. Yang, H.; Valenzuela, S.O.; Chshiev, M.; Couet, S.; Dieny, B.; Dlubak, B.; Fert, A.; Garello, K.; Jamet, M.; Jeong, D.E.; et al. Two-dimensional materials prospects for non-volatile spintronic memories. *Nature* **2022**, *606*, 663–673. [\[CrossRef\]](#)
4. Santos, T.S.; Mihajlovic, G.; Smith, N.; Li, J.L.; Carey, M.; Katine, J.A.; Terris, B.D. Ultrathin perpendicular free layers for lowering the switching current in STT-MRAM. *J. Appl. Phys.* **2020**, *128*, 113904. [\[CrossRef\]](#)
5. Pandey, N.; Chauhan, Y.S. Multidomain interactions in perpendicular magnetic tunnel junction (p-MTJ): Enabling multistate MRAM. *IEEE Trans. Electron Devices* **2023**, *70*, 2304–2311. [\[CrossRef\]](#)
6. Pashen'kin, I.Y.; Sapozhnikov, M.V.; Gusev, N.S.; Rogov, V.V.; Tatarskii, D.A.; Fraerman, A.A.; Volochaev, M.N. Magnetoelectric effect in CoFeB/MgO/CoFeB magnetic tunnel junctions. *JETP Lett.* **2020**, *111*, 690–693. [\[CrossRef\]](#)
7. Aull, T.; Şaşıoğlu, E.; Hinsche, N.F.; Mertig, I. Ab initio study of magnetic tunnel junctions based on half-metallic and spin-gapless semiconducting heusler compounds: Reconfigurable diode and inverse tunnel-magnetoresistance effect. *Phys. Rev. Applied* **2022**, *18*, 034024. [\[CrossRef\]](#)
8. Atasoyu, M.; Altun, M.; Ozoguz, S. Sensing schemes for STT-MRAMs structured with high TMR in low RA MTJs. *Microelectron. J.* **2019**, *89*, 30–36. [\[CrossRef\]](#)
9. Elmen, G.W. Magnetic alloys of iron, nickel, and cobalt. *Bell Syst. Tech. J.* **1929**, *8*, 435–465. [\[CrossRef\]](#)
10. Parra, C.; Perea, C.D.; Bolivar, F.J. Effect of cobalt addition on the microstructural evolution, thermal stability and magnetic properties of Fe-based amorphous alloys. *Vacuum* **2019**, *169*, 108911. [\[CrossRef\]](#)
11. Akhtar, M.; Khajuria, A. Effects of prior austenite grain size on impression creep and microstructure in simulated heat affected zones of boron modified P91 steels. *Mater. Chem. Phys.* **2020**, *249*, 122847. [\[CrossRef\]](#)
12. Golovnia, O.A.; Popov, A.G.; Vlasova, N.I.; Protasov, A.V.; Gaviko, V.S.; Popov, V.V., Jr.; Kashyap, A. Effect of additions of phosphorous, boron, and silicon on the structure and magnetic properties of the melt-spun FePd ribbons. *J. Magn. Magn. Mater.* **2019**, *481*, 212–220. [\[CrossRef\]](#)
13. Chabi, T.; Bensebaa, N.; Alleg, S.; Azzaza, S.; Suñol, J.J.; Hlil, E.K. Effect of the boron content on the amorphization process and magnetic properties of the mechanically alloyed Fe_{92-x}Nb₈B_x Powders. *J. Supercond. Nov. Magn.* **2019**, *32*, 893–901. [\[CrossRef\]](#)
14. Hashim, M.; Ahmed, A.; Ali, S.A.; Shirsath, S.E.; Ismail, M.M.; Kumar, R.; Kumar, S.; Meena, S.S.; Ravinde, D. Structural, optical, elastic and magnetic properties of Ce and Dy doped cobalt ferrites. *J. Alloys Compd.* **2020**, *834*, 150089. [\[CrossRef\]](#)
15. Hussain, G.; Ahmed, I.; Rehman, A.U.; Subhani, M.U.; Morley, N.; Akhtar, M.; Arshad, M.I.; Anwar, H. Study of the role of dysprosium substitution in tuning structural, optical, electrical, dielectric, ferroelectric, and magnetic properties of bismuth ferrite multiferroic. *J. Alloys Compd.* **2022**, *919*, 165743. [\[CrossRef\]](#)
16. Pashkevich, A.V.; Fedotov, A.K.; Poddenezhny, E.N.; Bliznyuk, L.A.; Fedotova, J.A.; Basov, N.A.; Kharchanka, A.A.; Zukowski, P.; Koltunowicz, T.N.; Korolik, O.V.; et al. Structure, electric and thermoelectric properties of binary ZnO-based ceramics doped with Fe and Co. *J. Alloys Compd.* **2022**, *895*, 162261. [\[CrossRef\]](#)
17. Zukowski, P.; Koltunowicz, T.N.; Czarnacka, K.; Fedotov, A.K.; Tyschenko, I.E. Carrier transport and dielectric permittivity of SiO₂ films containing ion-beam synthesized InSb nanocrystals. *J. Alloys Compd.* **2020**, *846*, 156482. [\[CrossRef\]](#)
18. Fedotova, V.V.; Bushinsky, M.V.; Fedotov, A.K.; Pashkevich, A.V.; Larkin, A.V.; Nikitin, A.V.; Kozlenko, D.P. Structure, magnetic and electrical properties of Tb_{0.5}Nd_{0.5}CoO₃ perovskite solid solutions with carbon material flakes (CMF). *J. Alloys Compd.* **2023**, *925*, 171289. [\[CrossRef\]](#)
19. Koltunowicz, T.N.; Zhukowski, P.; Bondariev, V.; Saad, A.; Fedotova, J.A.; Fedotov, A.K. Enhancement of negative capacitance effect in (CoFeZr)_x(CaF₂)_(100-x) nanocomposite films deposited by ion beam sputtering in argon and oxygen atmosphere. *J. Alloys Compd.* **2014**, *615*, S361–S365. [\[CrossRef\]](#)
20. Diedkova, K.; Pogrebnjak, A.D.; Kyrylenko, S.; Smyrnova, K.; Buranich, V.V.; Horodek, P.; Zukowski, P.; Koltunowicz, T.N.; Galaszkiwicz, P.; Makashina, K.; et al. Polycaprolactone–MXene Nanofibrous Scaffolds for Tissue Engineering. *ACS Appl. Mater. Interfaces* **2023**, *15*, 14033–14047. [\[CrossRef\]](#)
21. Boiko, O.; Koltunowicz, T.N.; Zukowski, P.; Fedotov, A.K.; Larkin, A.V. The effect of sputtering atmosphere parameters on dielectric properties of the ferromagnetic alloy–ferroelectric ceramics nanocomposite (FeCoZr)_x(PbZrTiO₃)_(100-x). *Ceram. Int.* **2017**, *43*, 2511–2516. [\[CrossRef\]](#)
22. Zukowski, P.; Koltunowicz, T.N.; Bondariev, V.; Fedotov, A.K.; Fedotova, J.A. Determining the percolation threshold for (FeCoZr)_x(CaF₂)_(100-x) nanocomposites produced by pure argon ion-beam sputtering. *J. Alloys Compd.* **2016**, *683*, 62–66. [\[CrossRef\]](#)
23. Jemli, S.; Pinto, D.; Kanhounon, W.G.; Amara, F.B.; Sellaoui, L.; Petriciolet, A.B.; Dhaouadi, F.; Ameri, R.; Silva, L.F.O.; Bejar, S.; et al. Green β-cyclodextrin nanosponges for the efficient adsorption of light rare earth elements: Cerium and lanthanum. *J. Chem. Eng.* **2023**, *466*, 143108. [\[CrossRef\]](#)
24. Bulai, G.; Trandafir, V.; Irimiciuc, S.A.; Ursu, L.; Focsa, C.; Gurlui, S. Influence of rare earth addition in cobalt ferrite thin films obtained by pulsed laser deposition. *Ceram. Int.* **2019**, *45*, 20165–20171. [\[CrossRef\]](#)
25. Martin, E.; Grenier, S.; Barre, S.; Versini, G.; Blanc, N.; Boudet, N.; Roulland, F.; Pourroy, G.; Viart, N.; Lefèvre, C. Deleterious effect of rare earth elements substitution on the auxetic behavior of CoFe₂O₄ thin films. *J. Alloys Compd.* **2023**, *935*, 168082. [\[CrossRef\]](#)

26. Mattern, M.; Pudell, J.E.; Dumesnil, K.; Reppert, A.V.; Bargheer, M. Towards shaping picosecond strain pulses via magnetostrictive transducers. *Photoacoustics* **2023**, *30*, 100463. [[CrossRef](#)]
27. Deneff, J.I.; Rohwer, L.E.; Butler, K.S.; Kaehr, B.; Vogel, D.J.; Luk, T.S.; Reyes, R.A.; Cruz-Cabrera, A.A.; Martin, J.E.; Sava Gallis, D.F. Orthogonal luminescence lifetime encoding by intermetallic energy transfer in heterometallic rare-earth MOFs. *Nat. Commun.* **2023**, *14*, 981. [[CrossRef](#)] [[PubMed](#)]
28. Kaiser, C.; Parkin, S.S.P. High negative tunneling magnetoresistance in magnetic tunnel junctions with a ferrimagnetic CoFe–Gd electrode and a CoFe interface layer. *Appl. Phys. Lett.* **2006**, *88*, 112511. [[CrossRef](#)]
29. Bellouard, C.; George, B.; Marchal, G.; Maloufi, N.; Eugène, J. Influence of the thickness of the CoFe layer on the negative spin-valve effect in CoFe/Ag/CoFeGd trilayers. *J. Magn. Magn. Mater.* **1997**, *165*, 312–315. [[CrossRef](#)]
30. Saito, Y.; Kholid, F.N.; Karashtin, E.; Pashenkin, I.; Mikhaylovskiy, R.V. Emission spectroscopy of exchange-biased spintronic heterostructures: Single- and double-pump techniques. *Phys. Rev. Appl.* **2023**, *19*, 064040. [[CrossRef](#)]
31. Gayen, A.; Modak, R.; Srinivasan, A.; Srinivasu, V.V.; Alagarsamy, P. Thickness dependent magneto-static and magneto-dynamic properties of CoFeB thin films. *J. Vac. Sci. Technol. A* **2019**, *37*, 031513. [[CrossRef](#)]
32. Grassi, M.; Geilen, M.; Louis, D.; Mohseni, M.; Brächer, T.; Hehn, M.; Stoeffler, D.; Bailleul, M.; Pirro, P.; Henry, Y. Slow-wave-based nonmagnonic diode. *Phys. Rev. Appl.* **2020**, *14*, 024047. [[CrossRef](#)]
33. Meng, H.; Lum, W.H.; Sbiaa, R.; Lua, S.Y.H.; Tan, H.K. Annealing effects on CoFeB–MgO magnetic tunnel junctions with perpendicular anisotropy. *J. Appl. Phys.* **2011**, *110*, 033904. [[CrossRef](#)]
34. Vértesy, G.; Gasparics, A.; Griffin, J.M.; Mathew, J.; Fitzpatrick, M.E.; Uytendhouwen, I. Analysis of surface roughness influence in non-destructive magnetic measurements applied to reactor pressure vessel steels. *Appl. Sci.* **2020**, *10*, 8938. [[CrossRef](#)]
35. Favieres, C.; Vergara, J.; Madurga, V. Surface roughness influence on Néel-, crosstie, and bloch-type charged zigzag magnetic domain walls in nanostructured Fe films. *Materials* **2020**, *13*, 4249. [[CrossRef](#)]
36. Nowicki, R.; Świercz, R.; Świercz, D.O.; Rozenek, M. Experimental investigation of technological indicators and surface roughness of hastelloy C-22 after electrical discharge machining using POCO graphite electrodes. *Materials* **2022**, *15*, 5631. [[CrossRef](#)] [[PubMed](#)]
37. Vasiliu, R.D.; Porojan, S.D.; Bîrdeanu, M.I.; Porojan, L. Effect of thermocycling, surface treatments and microstructure on the optical properties and roughness of CAD-CAM and heat-pressed glass ceramics. *Materials* **2020**, *13*, 381. [[CrossRef](#)] [[PubMed](#)]
38. Kroker, M.; Souček, P.; Šlapanská, M.; Sochora, V.; Jílek, M.; Vašina, P. Predicting the composition of W-B-C coatings sputtered from industrial cylindrical segmented target. *Surf. Coat. Technol.* **2022**, *438*, 128411. [[CrossRef](#)]
39. Ma, K.; Chung, T.S.; Good, R.J. Surface energy of thermotropic liquid crystalline polyesters and polyesteramide. *J. Polym. Sci.* **1998**, *36*, 2327–2337. [[CrossRef](#)]
40. Owens, D.K.; Wendt, R.C. Estimation of the surface free energy of polymers. *J. Appl. Polym. Sci.* **1969**, *13*, 1741–1747. [[CrossRef](#)]
41. Kaelble, D.H.; Uy, K.C. A Reinterpretation of Organic Liquid-Polytetrafluoroethylene Surface Interactions. *J. Adhes.* **1970**, *2*, 50–60. [[CrossRef](#)]
42. Sreethawong, T.; Chavadej, S.; Ngamsinlapasathian, S.; Yoshikawa, S. A simple route utilizing surfactant-assisted templating sol-gel process for synthesis of mesoporous Dy₂O₃ nanocrystal. *J. Colloid Interface Sci.* **2006**, *300*, 219–224. [[CrossRef](#)]
43. Zied, B.M.A.; Asiri, A.M. Synthesis of Dy₂O₃ nanoparticles via hydroxide precipitation: Effect of calcination temperature. *J. Rare Earths* **2014**, *32*, 259–264. [[CrossRef](#)]
44. Liu, W.J.; Chang, Y.H.; Chen, Y.T.; Chiang, Y.C.; Liu, Y.C.; Wu, T.H.; Chi, P.W. Effect of annealing on the structural, magnetic, surface energy of CoFeBY films on Si (100) substrate. *Materials* **2021**, *14*, 987. [[CrossRef](#)] [[PubMed](#)]
45. Lan, T.T.B.; Chang, C.W.; Kuo, M.R.; Sun, A.A.C. Strengthening the magnetic properties of Pr-Fe-B thin films using biased substrate. *Colloids Surf. A Physicochem. Eng. Asp.* **2022**, *646*, 128925.
46. Ikeda, H.; Iwai, M.; Nakajima, D.; Kikuchi, T.; Natsui, S.; Sakaguchi, N.; Suzuki, R.O. Nanostructural characterization of ordered gold particle arrays fabricated via aluminum anodizing, sputter coating, and dewetting. *Appl. Sur. Sci.* **2019**, *465*, 747–753. [[CrossRef](#)]
47. Vasiliev, M.; Alam, M.N.E.; Alameh, K.; Premchander, P.; Lee, Y.T.; Kotov, V.A.; Lee, Y.P. Annealing behaviour and crystal structure of RF-sputtered Bi-substituted dysprosium iron-garnet films having excess co-sputtered Bi-oxide content. *J. Phys. D* **2011**, *44*, 075002. [[CrossRef](#)]
48. Yang, S.Y.; Chien, J.J.; Wang, W.C.; Yu, C.Y.; Hing, N.S.; Hong, H.E.; Hong, C.Y.; Yang, H.C.; Chang, C.F.; Lin, H.Y. Magnetic nanoparticles for high-sensitivity detection on nucleic acids via superconducting-quantum-interference-device-based immunomagnetic reduction assay. *J. Magn. Magn. Mater.* **2011**, *323*, 681–685. [[CrossRef](#)]
49. Jalili, H.; Aslibeiki, B.; Varzaneh, A.G.; Chernenko, V.A. The effect of magneto-crystalline anisotropy on the properties of hard and soft magnetic ferrite nanoparticles. *Beilstein J. Nanotechnol.* **2019**, *10*, 1348–1359. [[CrossRef](#)]
50. Frajer, G.; Isnard, O.; Chazal, H.; Delette, G. Effect of cobalt addition on the magneto-crystalline anisotropy parameter of sintered NiZn ferrites evaluated from magnetization curves. *J. Magn. Magn. Mater.* **2019**, *473*, 92–98. [[CrossRef](#)]
51. Wen, D.; Li, J.; Gan, G.; Yang, Y.; Zhang, H.; Liu, Y. Double peaks of the permeability spectra of obliquely sputtered CoFeB amorphous films. *Mater. Res. Bull.* **2019**, *110*, 107–111. [[CrossRef](#)]
52. Kamarád, J.; Arnold, Z. Effect of hydrostatic pressure on magneto-crystalline anisotropy of Heusler Ni₂MnSn-based alloy. *High Press. Res.* **2021**, *41*, 405–413. [[CrossRef](#)]

53. Ke, R.; Hu, C.; Zhong, M.; Wan, X.; Wu, K. Grain refinement strengthening mechanism of an austenitic stainless steel: Critically analyze the impacts of grain interior and grain boundary. *J. Mater. Res. Technol.* **2022**, *17*, 2999–3012. [[CrossRef](#)]
54. Kotan, H.; Tekin, M.; Bayatlı, A.; Bayrak, K.G.; Kocabaş, M.; Ayas, E. Effect of in-situ formed oxide and carbide phases on microstructure and corrosion behavior of Zr/Y doped CoCrFeNi high entropy alloys prepared by mechanical alloying and spark plasma sintering. *Intermetallics* **2023**, *162*, 107998. [[CrossRef](#)]
55. Krbal, M.; Prikryl, J.; Pis, I.; Prokop, V.; Pereira, J.R.; Kolobov, A.V. Anomalous electrical conductivity change in MoS₂ during the transition from the amorphous to crystalline phase. *Ceram. Int.* **2023**, *49*, 2619–2625. [[CrossRef](#)]
56. Mazur, M.; Lubańska, A.; Domaradzki, J.; Wojcieszak, D. Complex research on amorphous vanadium oxide thin films deposited by gas impulse magnetron sputtering. *Appl. Sci.* **2022**, *12*, 8966. [[CrossRef](#)]
57. Lebedev, A.A.; Davydov, S.Y.; Roenkov, A.D.; Lebedev, S.P.; Puzyk, M.; Klotchenko, S.; Usikov, A.S. Graphene on SiC substrate as biosensor: Theoretical background, preparation, and characterization. *Materials* **2021**, *14*, 590. [[CrossRef](#)]
58. Zahler, M.P.; Kraschewski, S.M.; Störmer, H.; Gerthsen, D.; Bäurer, M.; Rheinheimer, W. Grain growth and segregation in Fe-doped SrTiO₃: Experimental evidence for solute drag. *J. Eur. Ceram.* **2023**, *43*, 1613–1624. [[CrossRef](#)]
59. Schössler, T.; Schön, F.; Lemier, C.; Urban, G. Effect of high temperature annealing on resistivity and temperature coefficient of resistance of sputtered platinum thin films of SiO₂/Pt/SiO_x interfaces. *Thin Solid Films* **2020**, *698*, 137877. [[CrossRef](#)]
60. Pandey, M.K.; Kar, A.K. Nickel concentration dependent evolution of magnetic domain structures in electrodeposited carbon composite thin films. *J. Magn. Magn. Mater.* **2020**, *506*, 166801. [[CrossRef](#)]
61. Navarro, E.; González, M.U.; Béron, F.; Tejo, F.; Escrig, J.; Martín, J.M.G. Large-area nanopillar arrays by glancing angle deposition with tailored magnetic properties. *Nanomater.* **2022**, *12*, 1186. [[CrossRef](#)] [[PubMed](#)]
62. Giuliano, D.; Gnoli, L.; Ahrens, V.; Roch, M.R.; Becherer, M.; Turvani, G.; Vacca, M.; Riente, F. Ga⁺ ion irradiation-induced tuning of artificial pinning sites to control domain wall motion. *ACS Appl. Electron. Mater.* **2023**, *5*, 985–993. [[CrossRef](#)]
63. Hennessey, G.; Peters, T.; Tipsawat, P.; Checa, M.; Collins, L.; McKinstry, S.T. Domain wall motion across microstructural features in polycrystalline ferroelectric films. *Acta Mater.* **2023**, *250*, 118871. [[CrossRef](#)]
64. Alhosseini, F. Investigation of corrosion and tribological characteristics of annealed CrN/CrAlN coatings deposited by CAE-PVD. *Ceram. Int.* **2023**, *49*, 3016–3029.
65. Misyura, S.Y.; Andryushchenko, V.A.; Morozov, V.S. The influence of copper substrate temperature on the wettability of graphene coating. *Surf. Innov.* **2023**, *11*, 272–284. [[CrossRef](#)]
66. Madadi, F.; Rezaeian, A.; Edris, H.; Zhiani, M. Influence of surface roughness and hydrophobicity of bipolar plates on PEM performance. *Surf. Coat. Technol.* **2020**, *389*, 125676. [[CrossRef](#)]
67. Sharma, P.; Ponte, F.; Lim, M.J.; Figueiredo, N.M.; Ferreira, J.; Carvalho, S. Plasma etching of polycarbonate surfaces for improved adhesion of Cr coatings. *Appl. Surf. Sci.* **2023**, *637*, 157903. [[CrossRef](#)]
68. Lacmanova, V.; Leitner, J.; Hausild, P.; Cech, J.; Nohava, J.; Sajdl, P.; Michalcova, A.; Slepicka, P.; Reznickova, A. Annealing of Cu nanolayers on glass: Structural, mechanical and thermodynamic analysis. *Vacuum* **2023**, *212*, 111991. [[CrossRef](#)]
69. Zhang, Y.; Sui, Y.; Jiang, Y.; Han, L. Effect of Dy₂O₃ content on microstructure and mechanical properties of zirconia-toughened alumina. *Ceram. Int.* **2022**, *48*, 23206–23212. [[CrossRef](#)]
70. Renk, O.; Hohenwarter, A.; Kiener, V.M.; Pippan, R. Exploring the anneal hardening phenomenon in nanocrystalline Pt-Ru alloys. *J. Alloys Compd.* **2023**, *935*, 168005. [[CrossRef](#)]
71. Kushwaha, A.K.; John, M.; Misra, M.; Menezes, P.L. Nanocrystalline materials: Synthesis; characterization; properties; applications. *Crystals* **2021**, *11*, 1317. [[CrossRef](#)]
72. Reis, F.D.A.A. Effects of film growth kinetics on grain coarsening and grain shape. *Phys. Rev. E* **2017**, *95*, 042805. [[CrossRef](#)] [[PubMed](#)]
73. Liu, W.J.; Chang, Y.H.; Chiang, C.C.; Chen, Y.T.; Wang, Y.Z.; Wu, C.L.; Lin, S.H.; Ou, S.L. Thickness, annealing, and surface roughness effect on magnetic and significant properties of Co₄₀Fe₄₀B₁₀Dy₁₀ thin films. *Materials* **2023**, *16*, 5995. [[CrossRef](#)] [[PubMed](#)]
74. Kharmouche, A.; Cherif, S.M.; Bourzami, A.; Layadi, A.; Schmerber, G. Structural and magnetic properties of evaporated Co/Si(100) and Co/glass thin films. *J. Phys. D* **2004**, *37*, 2583–2587. [[CrossRef](#)]

Disclaimer/Publisher's Note: The statements, opinions and data contained in all publications are solely those of the individual author(s) and contributor(s) and not of MDPI and/or the editor(s). MDPI and/or the editor(s) disclaim responsibility for any injury to people or property resulting from any ideas, methods, instructions or products referred to in the content.